Eur. Phys. J. Plus (2018) **133**: 306
DOI 10.1140/epjp/i2018-12135-6

THE EUROPEAN PHYSICAL JOURNAL PLUS

Regular Article

# Simulating phase change during the droplet deformation and impact on a wet surface in a square microchannel: An application of oil drops collision

A. Asadollahi[1], S. Rashidi[2], J.A. Esfahani[3], and R. Ellahi[4,a]

[1] Department of Mechanical Engineering & Energy Processes, Southern Illinois University, Carbondale, IL 62901, USA
[2] Department of Mechanical Engineering, Semnan Branch, Islamic Azad University, Semnan, Iran
[3] Department of Mechanical Engineering, Ferdowsi University of Mashhad, Mashhad 91775-1111, Iran
[4] Department of Mathematics & Statistics, FBAS, IIUI, 44000 Islamabad, Pakistan

Received: 29 May 2018 / Revised: 25 June 2018
Published online: 3 August 2018


**Abstract.** This paper is an attempt to simulate the mathematical modelling on drop deformation in a saturated medium due to its movement and collision onto the liquid film. The reactions between fluid-fluid interaction and wall are completely simulated. Computations are performed for a two-dimensional domain under the influence of a saturation situation (that is saturation vapor and liquid co-exist) by the lattice Boltzmann method. The effects of different parameters, such as Weber number, collision angle on the drop deformation and its collision onto the liquid film, radius and initial position of the droplet are investigated. A stronger wave forms in the liquid film after collision of the drop for the case of inclined collision in comparison with the normal one. Additionally, a 5.5% increment in the maximum height of the created wave for $R_{\mathrm{dp}} = 22$ Lu and normal collision when the initial position of the drop moves from $H = 0.5\,\mathrm{L}$ to $H = 0.25\,\mathrm{L}$ is found.

## 1 Introduction

Recently, the drop impact process and droplet formation are widely used in various industrial applications containing oil drops collision on surfaces of the combustion chambers, salty drops collision on thermal pipes in horizontal-pipe dropping layer evaporators, chemical processes, boiling systems, spraying cooling, emulsification, raindrop formation, combustion of fuel sprays, spray coating, and waste treatment [1–3]. According to the various applications, the drop collision occurs on a dry or wetted surface or a liquid film. Many researchers in the last decade devoted their efforts on drop collisions on a dry wall. For instance, Chandra *et al.* [4] studied the clash dynamics of a droplet on a solid metallic wall. They employed a flash photographic technique. By focusing on the clear images of the droplet structure during the deformation procedure, they found that the maximum diameter of liquid that spreads on the wall is in agreement with the predictions of a simplified technique. Fukai *et al.* [5] theoretically and experimentally studied the deformation of a spherical droplet impacting with a flat wall. They showed that the maximum splat radius reduces as the value of the advancing contact angle increases. Francois and Shyy [6] have numerically investigated the effects of motion of a droplet on a flat dry wall. They used the immersed boundary technique. They performed simulations for static and dynamic contiguity angles. They found that the contiguity angle has influence on the recoiling and spreading processes. Fujimoto *et al.* [7] used the flash photography technology to investigate the clash of water drops with a warm Inconel 625 alloy wall. They observed a weak boiling at the joint surface between two phases when clashing the droplet with the solid at temperature equal to 170 °C. Moreover, numerous vapour bubbles were formed for the temperatures in the range of 200 to 300 °C. Mitra *et al.* [8] investigated the impact of a subcooled droplet on a spherical wall with large thermal conductivity. Their results indicated that the droplet disintegration and rebound phenomena occur at higher and lower values of the Weber number, respectively.

Besides, there are few studies on the drop clash on a wetted wall or a liquid layer available in the literature. Manzello *et al.* [9] presented an experimental study for the water droplet impingement on a liquid layer. They found

[a] e-mail: rahmatellahi@yahoo.com (corresponding author)

that there is a considerable difference between the clash dynamics of water in the HFE7100 pool with the water droplet impingement on a water pool. Cossali *et al.* [10] studied experimentally the clash of a drop on a wetted surface. They found that the jet diameter increases with time. This may be as a result of the increment in the rim generated by a partial re-absorption of the liquid creating the crown. Rioboo *et al.* [11] carried out an experimental work on the splash and crown creation pending single droplet clash on humid walls. Nikolopoulos *et al.* [12] carried out a 3D numerical work on a drop exceeding normally to the surface layer. They utilized the finite volume with volume of fluid techniques and used an adaptive local grid refinement method to track the joint surface between liquid and gas phases with higher accuracy. Okawa *et al.* [13] studied experimentally the normal clash of water drops on a plane water layer. They found that the number of secondary drops augments with the impact $K$-number ($= \mathrm{We}\ \mathrm{Oh}^{-0.4}$), where We and Oh are Weber and the Ohnesorge numbers, respectively. Marengo *et al.* [14] studied the drop collisions with simple and complex surfaces. They considered the effects of morphological and wettability in it. Liang *et al.* [15] examined the liquid layer behaviours during a droplet clash on humid cylindrical walls. They concluded that the liquid layer height augments significantly with the increase in Weber number or with the decrease in the cylinder-drop curvature ratio. Recently, Liang *et al.* [16] investigated the hydrothermal characteristic during a droplet clash on a liquid layer with an underneath wall with small temperature. They classified the liquid inside the film in to three parts containing the impact, transition, and static parts. They found that the mean surface heat flux augments as the clash speed increases, while the influences of layer width and drop size are negligible. One can find few more useful techniques to investigate a problem similar to that under consideration including dipolar porous and micropolar porous media [17–20]. But, recently, the Lattice Boltzmann method (LBM) has been considered as a good technique for simulation of a large number of problems with complex fluid flow. The capability to easily represent intricate physical phenomena, memory management, and modelling in intricate geometries are some benefits of this technique [21,22]. Esfahani and Norouzi [23] used the lattice Boltzmann equation to investigate the gas flow in a micro-/nano-channel for rarefied gas flows. They reported that this equation could satisfactorily predict the Knudsen minimum effect. Some researchers used this technique to simulate the multiphase flows. Sbragaglia *et al.* [24] suggested an approach based on the lattice Boltzmann equation to describe the multiphase flows in nano- and micro-corrugated devices. They investigated the significance of concerting influences of hydrophobicity on the mass flow rate in a micro-duct. Cates *et al.* [25] reviewed some applications of LBM to investigate the hydrodynamics of fluid crystalline matters. Especially, they focused on the active gels and blue phases. Liu *et al.* [26] investigated the pancake bouncing on super-hydrophobic surfaces. Leclaire *et al.* [27] used a multiphase LBM to simulate dynamics between liquid phases. Many investigators employed lattice Boltzmann method (LBM) to model condensation, phase-change processes and liquid removal from micro objects [28,29]. Alapati *et al.* [30] used LBM to study the 3D droplet creation in a cross-junction micro-duct. The computed results showed that the droplets are smoothly created in the junction section of the micro-duct. In another study, Huang *et al.* [31] studied the droplet movement inside a wavy duct by employing LBM. They reported that the droplet transfers with higher speed along a wavy hydrophobic wall than on their hydrophilic surfaces. Wang *et al.* [32] simulated the droplet generation in micro-ducts with the LBM. This research showed that the multiphase flows in micro-ducts has a high sensitivity to the small difference in terms of duct geometry. Fu *et al.* [33] employed the multiphase LBM to model the dynamic characteristic of droplets of condensation on walls. This research indicated that the droplets trap around micro ridges with large distance and altitude. A numerical study on the dynamics of drop in a PEM fuel cell microduct has been performed by Amara and Nasrallah [34]. They used the LBM to simulate this problem. They found that the drop deformation augments with increasing the capillary number. The capillary number presents a rivalry between the frictional and capillary forces in this paper. Zi-yuan *et al.* [35] employed the lattice Boltzmann technique to simulate a three-dimensional drop falling down onto a liquid layer. They used the single-phase free surface tracking method and supposed that the gas phase has little effect on the liquid one. Recently, Fallah kharmiani *et al.* [36] simulated a droplet collision on a liquid layer. They did not discuss about the collision angles in their work.

Keeping the aforementioned studies in mind, one can easily perceive that the behaviour of a droplet near the surface with promising deformation along with the dropping possibility is an important topic for investigation. Consequently, in this paper, a comprehensive study is offered on the collision of a drop to the liquid surface especially for the collision of the drop on a fluid film with different angles and for the evaporation of droplets with smaller size before contacting the fluid film. The deformation of the drop during the motion, the evaporation of droplets and the disappearance of smaller droplets before the collision with the liquid surface, the effect of the collision of the droplet at different angles, and the behaviour of the surface of the liquid after the collision of the droplet are examined and discussed in detail. These features make the problem more real. Literature survey bears witness that there is no comprehensive study yet available in the existing literature which consider these features altogether. It is worth mentioning that removing the fluid produced in the unit after the condensation is a critical situation in micro-devices. It is found that before removing this liquid, the motion of droplets inside the device at different angles and their collision to the surface can be used for self-cleaning applications. Furthermore, the angled motion of the droplet leads to walk a longer path as compared with the straight one and this leads to remove more dust particles from the object. Accordingly, it is important to simulate the drop collision with different angles. To the best of the authors' knowledge, this simulation is performed in this research for the first time by means of the lattice Boltzmann method.

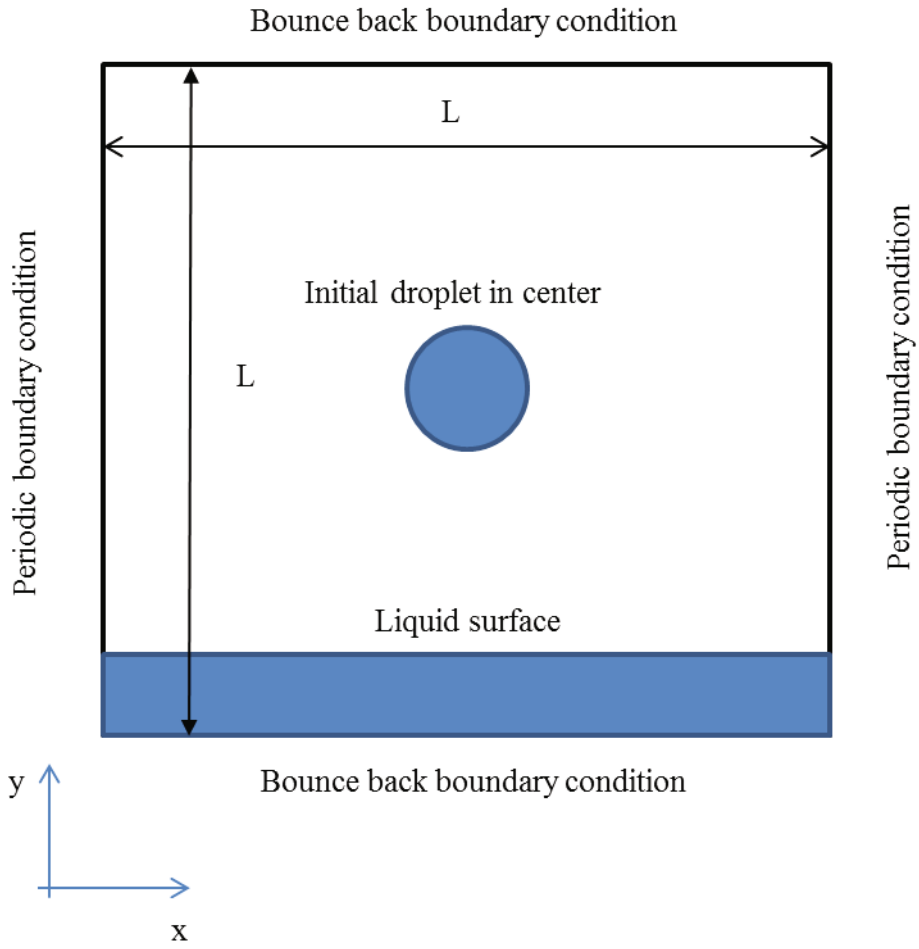


**Fig. 1.** Schematic of the computational domain, coordinate system with corresponding boundary conditions.

## 2 Problem statement

Figure 1 portrays the view of computational area, coordinate system and corresponding boundary conditions. A square area with sides of $L = 200$ Lu is plotted. The bounce back boundaries are utilized for the top and bottom sides. In addition, a periodic boundary is considered for lateral sides. A liquid layer with width of 20 Lu is located at the bottom surface of the domain. A drop with radius of $R_{\mathrm{dp}}$ is located inside the domain. It is assumed that the domain to be saturate.

## 3 Numerical procedure

### 3.1 Lattice Boltzmann method (LBM)

A LBM with pseudo potential procedure is utilized [37,38] in the current study. In LBM, the Boltzmann equation describes the statistical characteristic of the thermodynamic process. By considering Bhatnagar-Gross-Krook approximation [39] irrespective of outer forces, it is given by

$$f_i(x + e_i\delta t, t + \delta t) = f_i(x,t) + \frac{f_i^{eq}(x,t) - f_i(x,t)}{\tau}, \tag{1}$$

in which $f_i(x,t)$ indicates particle distribution function whereas $e$, $\delta t$ and $\tau$ indicate the discrete speed, time step and non-dimensional relaxation time, respectively. The Boltzmann-Maxwellian equilibrium distribution [40], $f^{eq}$ is defined by

$$f^{eq} = w_i\rho\left[1 + 3\frac{e_i \cdot u^{eq}}{c^2} + 9\frac{(e_i \cdot u^{eq})^2}{2c^4} - \frac{3u^{eq^2}}{2c^2}\right], \tag{2}$$

where $c$, $u_{eq}$, $w_i$, respectively, denote the characteristic speed, modified speed, and weight coefficients. However, the density $\rho$, is [41]

$$\rho = \sum_{i=0} f_i. \tag{3}$$

The discrete speeds are [42]:

$$\begin{aligned} e_0 &= 0, \\ e_{1-4} &= c(\cos(i-1)\pi/2, \sin(i-1)\pi/2), \\ e_{5-8} &= \sqrt{2}c(\cos(i-5)\pi/2 + \pi/4, \sin(i-5)\pi/2 + \pi/4). \end{aligned} \tag{4}$$

To obtain the discrete speeds, the $D_2Q_9$ model is utilized. Accordingly, the Weight coefficients, $w_i$, are [40,41]:

$$w_i = \begin{cases} 4/9, & \text{for } i = 0, \\ 1/9, & \text{for } i = 1,2,3,4, \\ 1/36, & \text{for } i = 5,6,7,8. \end{cases} \tag{5}$$

The kinematic viscosity, as given in [43], is

$$\upsilon = \left(\tau - \frac{1}{2}\right) C_s^2 \delta t, \tag{6}$$

where $C_s = c/\sqrt{3}$ denotes the sound velocity.

### 3.2 Pseudo potential procedure

In multiphase flows, the molecular interplays cause the phase separation. For mimicking molecular interplays, the interplay force is considered [44] by

$$F_{\text{int}}(x,t) = -G\psi(x,t) \sum_{i=1}^{8} w_i \psi(x + e_i \Delta t, t) e_i, \tag{7}$$

$G$ and $\psi$ indicate the interplay strength and interplay potential function respectively. The procedure of Shan and Chen [37] is utilized for the interplay potential function as below:

$$\psi(\rho) = \psi_0 \exp(-\rho_0/\rho), \tag{8}$$

$\psi_0$ and $\rho_0$ are optional constants. The negative quantities of interaction strength $G$, indicate absorption forces of the fluid molecules. The state equation by adding the particle-particle absorption force is given by [42]

$$P = \frac{\rho}{3} + \frac{G}{6}(\psi(\rho))^2. \tag{9}$$

There are various definitions which can be presented for $\psi(\rho)$, while based on the Shan-Chen model, the state equation is

$$P = \frac{\rho}{3} + \frac{G}{6}(\psi_0 \exp(-\rho_0/\rho))^2. \tag{10}$$

It should be noted that the vapor and liquid phases coexist at pressures lower than the critical pressure by considering this equation [42]. By using zero values for the first and second derivatives of eq. (10), $\rho_{\text{cr}}$ and $G_{\text{critical}}$ are determined as below:

$$\begin{aligned} \rho_{\text{cr}} &= \rho_0, \\ G_{\text{critical}} &= -\frac{\rho_0}{\psi_0^2} \exp(2). \end{aligned} \tag{11}$$

The characteristics of the critical point are obtained from the fact that the first and second derivatives of pressure with respect to density for the critical point should be zero. By using zero amounts for the first and second derivatives of eq. (10) with respect to density, the critical parameters can be achieved as eq. (11). $\rho_{\text{cr}}$ and $G_{\text{critical}}$ can be obtained from eq. (11) by considering the quantities of 200 and 4 for $\rho_0$ and $\psi_0$, respectively. Phase separation occurs for

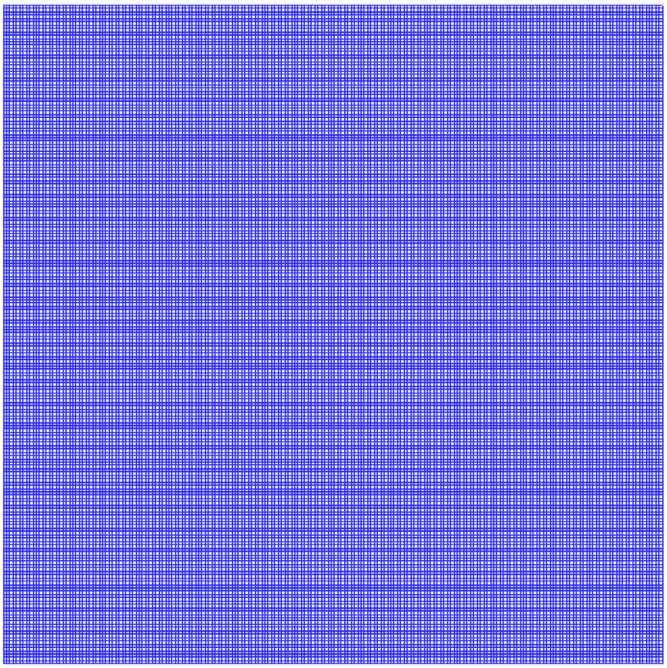

**Fig. 2.** Mesh distribution used in this research.

$G \leq G_{\text{critical}}$ [34]. Negative quantities of $G$ indicate the attraction of particles. The interplay force between the fluid molecules and wall, $F_{\text{ads}}$, is obtained as [43]

$$F_{\text{ads}}(x,t) = -G_{\text{ads}}\psi(x,t)\sum_{i=1}^{8} w_i s(x + e_i \Delta t, t) e_i, \tag{12}$$

here $G_{\text{ads}}$ indicates the adsorption coefficient. However, $s(x + e_i\Delta t, t)$ denotes a switch function. $s = 1$ is used for surface nodes, while $s = 0$ is considered for other nodes. The hydrophilic and hydrophobic walls are recognized by considering an adsorption coefficient. The wall is rather hydrophilic for larger amounts of $|G_{\text{ads}}|$. In addition, the corrected velocity, $u_{\text{eq}}$, is calculated by [44]

$$u_{\text{eq}} = u + \frac{\tau F}{\rho}, \tag{13}$$

$F$ denotes the total force and consists of $F_{\text{int}}$ and $F_{\text{ads}}$. However, the macroscopic speed of flow can be calculated as follows:

$$u = \frac{1}{\rho}\sum_{i=0} e_i f_i. \tag{14}$$

### 3.3 Boundary conditions

As stated formerly, the periodic condition is considered for side walls. These boundary conditions can be defined in the following form:

$$f(i,0,y) = f(i,L,y), \quad \text{for } i = 1,5,8, \tag{15}$$
$$f(i,L,y) = f(i,0,y), \quad \text{for } i = 3,6,7. \tag{16}$$

Moreover, the bounce-back condition is selected for the upper and lower boundaries. For the bottom surface of the domain, it is defined as

$$f_2 = f_4, \qquad f_5 = f_7, \qquad f_6 = f_8. \tag{17}$$

### 3.4 Grid sensitivity

Figure 2 shows the mesh considered for the computational domain. A square grid is considered. Three grid numbers are assayed to achieve an optimal grid. The influences of changes in grid size on the wet fraction are investigated and

**Table 1.** Effect of grid size on wet fraction at $t = 25600$.

| No. | Grid size | Wet fraction | Percentage difference |
|---|---|---|---|
| 1 | 100 Lu × 100 Lu | 33.65% | 4.42% |
| 2 | 200 Lu × 200 Lu | 38.07% | 0.92% |
| 3 | 400 Lu × 400 Lu | 37.15% | – |

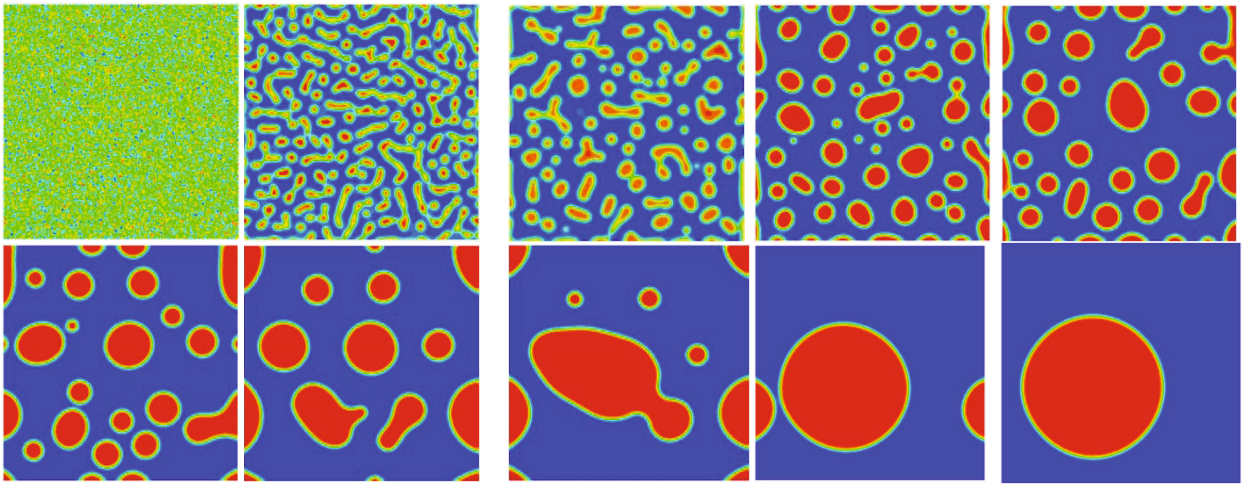

**Fig. 3.** Display of phase separation in different times ($t = 0, 100, 200, 400, 800, 1600, 3200, 6400, 12800$ and $25600$).

**Table 2.** Percent of wetness fraction at two values of non-dimensional time (6400 and 25600) as compared with a previous study.

| | Percent of wetness fraction ($t = 6400$) | Percent of wetness fraction ($t = 25600$) |
|---|---|---|
| Present study | 36.38% | 38.07% |
| Sukop and Thorne (2006) | 35.61% | 37.52% |
| Percentage error | 0.77% | 0.55% |

presented in table 1. This variable is measured by following expression:

$$Wet\ fraction = \frac{Water\ mass}{Vapor\ mass} \times 100. \tag{18}$$

The data of table 1 is obtained using image processing in Matlab and presented at $t = 25600$. It is found that the difference between grid sizes 200 Lu × 200 Lu and 400 Lu × 400 Lu is 0.92%. Accordingly, the grid size 200 Lu × 200 Lu is selected for computations.

### 3.5 Validity of the results

To evaluate the accuracy of LBM, the current results are contrasted with the data of Sukop [44]. The phase separations at different times in a duct are displayed at fig. 3. A density $\rho = 200 + rand$ is supposed for the initial quantity in the domain. A subroutine of random number in the FORTRAN compiler is utilized to initialize the *rand* variable for any grid of the computational area. A random number between 0 to 1 is considered for any grid in the current subroutine. Constant quantities of 4, 200, and −120 are selected for $\psi_0$, $\rho_0$, and $G_{\text{int}}$, respectively. An agreement between two studies can be found in fig. 3. In addition, the wetness fraction, $W$, at two values of time (*e.g.*, 6400 and 25600) are listed in table 2. Image processing is employed to measure this variable. It is concluded that the maximum difference of these studies is around 0.77%. This indicates good agreement between the present LBM and other results presented in the literature.

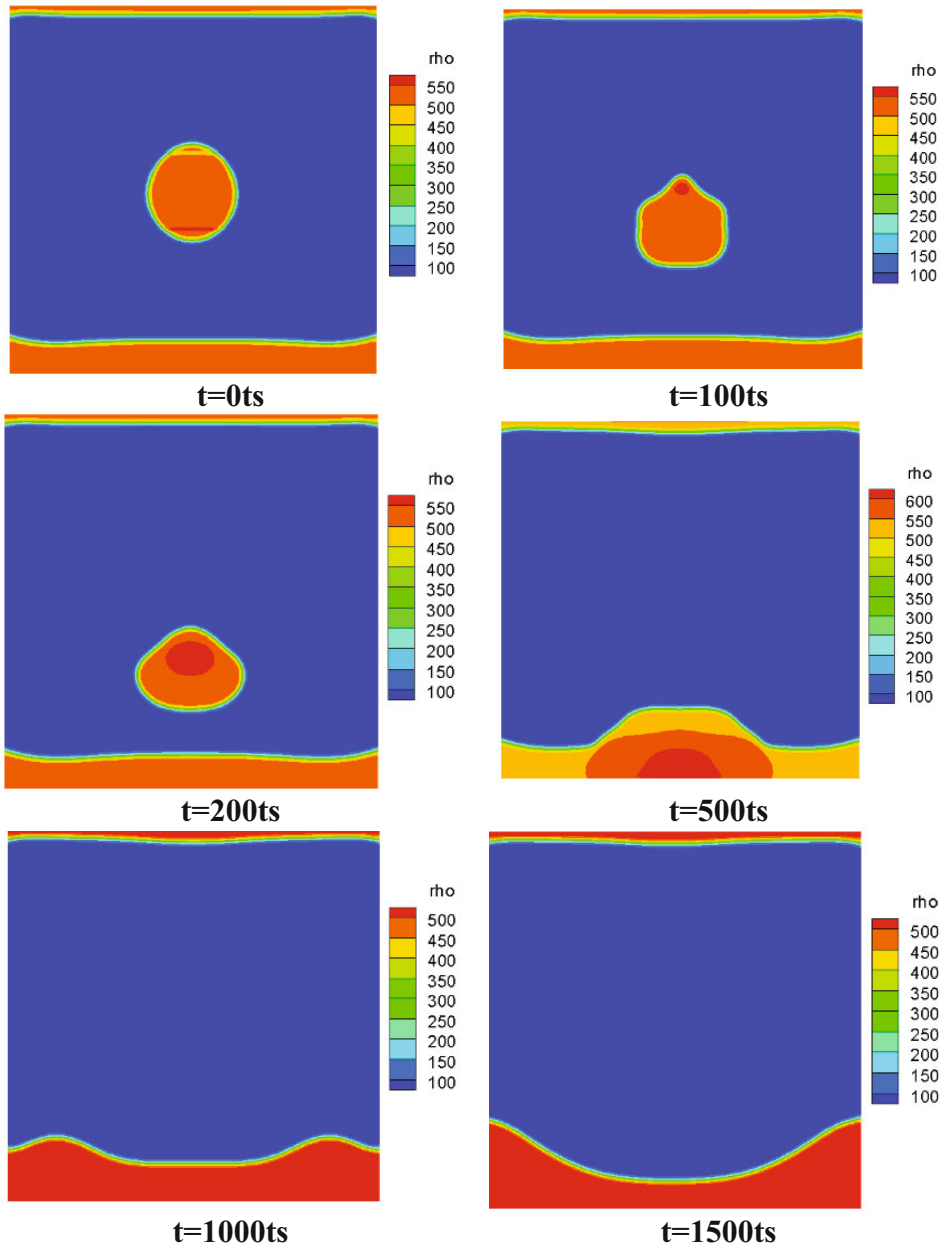


**Fig. 4.** Normal drop collision to the liquid surface at $R_{\mathrm{dp}} = 22\,\mathrm{Lu}$, initial normal velocity of the drop $= -0.2\,\mathrm{Lu/ts}$, We $= 59.5$, and $H = 0.5\,\mathrm{L}$ for different time steps.

## 4 Results and discussion

Figure 4 shows a normal drop collision to the liquid film at $R_{\mathrm{dp}} = 22\,\mathrm{Lu}$, $H = 0.5\,\mathrm{L}$, initial normal velocity of the droplet $= -0.2\,\mathrm{Lu/ts}$, and We $= 59.5$ for different time steps. $R_{\mathrm{dp}}$ and $H$ are the drop radius and the initial position of the drop, respectively. The change of the density is shown in color scale at the horizontal band located aside of any image. Moreover, the Weber number is defined as follows [45]:

$$\mathrm{We} = \frac{\rho v^2 l}{\sigma} = \frac{\rho v^2 2R_{\mathrm{dp}}}{\sigma}\,, \tag{19}$$

where $l$ is the characteristic length. The droplet diameter ($d_p$) is considered as the characteristic length ($l = d_p = 2R_p$). In addition, $R_{\mathrm{dp}}$, $v$, $\sigma$, and $\rho$ denote radius, velocity, surface tension and density of the drop, respectively.

It should be stated that the drop collides with the liquid film normally at $R_{\mathrm{dp}} = 22\,\mathrm{Lu}$ and We $= 59.5$ as in fig. 4. As mentioned earlier, a liquid layer with width 20 Lu is located at the bottom surface of the domain. Since the domain

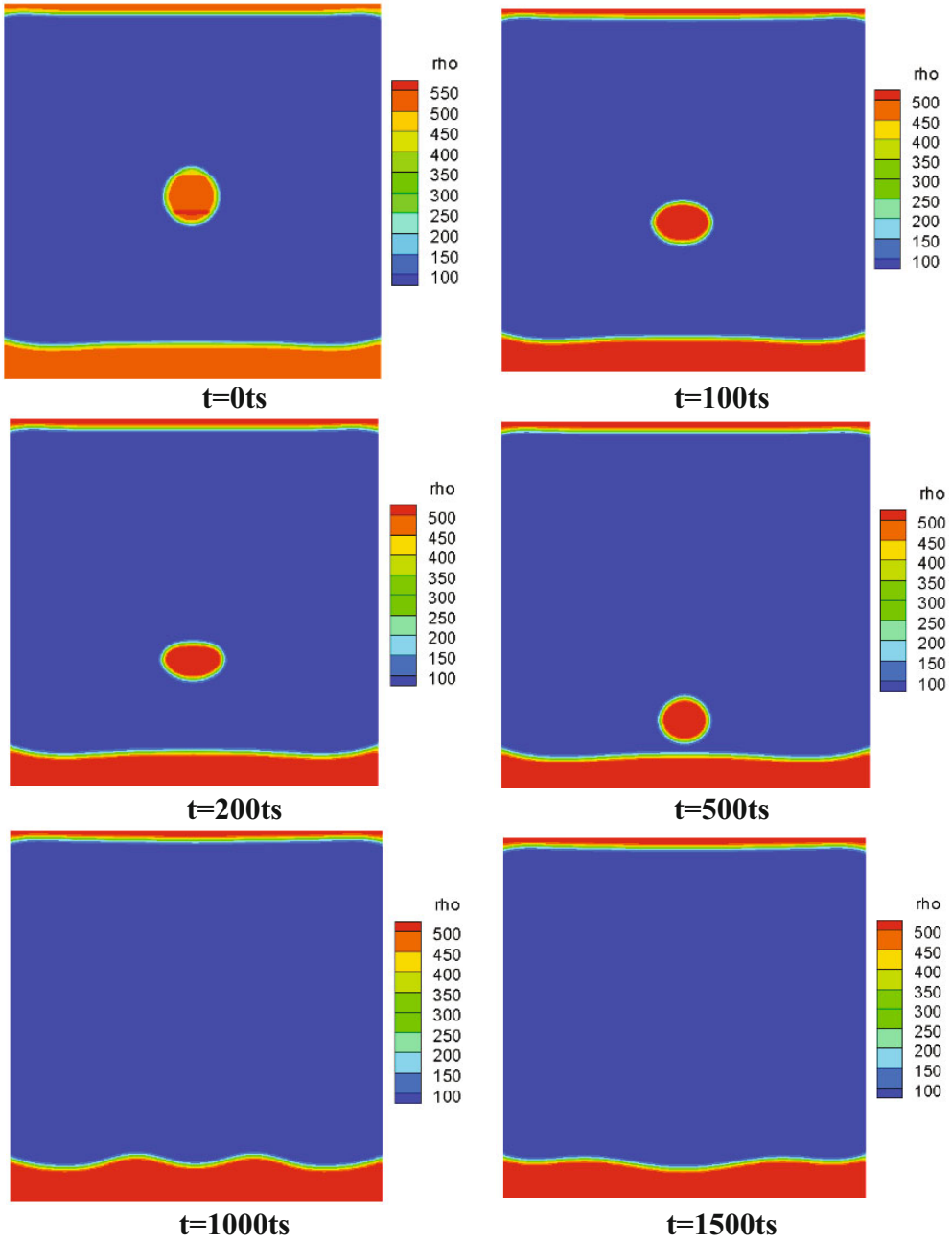


**Fig. 5.** Normal drop collision to the liquid surface at $R_{\mathrm{dp}} = 12\,\mathrm{Lu}$, initial normal velocity of the drop $= -0.2\,\mathrm{Lu/ts}$, We $= 32.5$, and $H = 0.5\,\mathrm{L}$ for different time steps.

is saturated, a thin liquid film is generated on the top surface of the domain. A vertical velocity is considered for drop at the initial time ($-0.2\,\mathrm{Lu/ts}$). This initial velocity leads to move the drop toward the liquid film. Firstly, this initial velocity deforms the drop at $t = 100\,\mathrm{ts}$. More deformations with the decrease in velocity occur for the drop by moving toward the bottom liquid film, due to the drag force on surface of the drop (see $t = 200\,\mathrm{ts}$). Note that the drag force on the surface of the drop is created by saturated steam in the domain. The drop collides with the liquid film at $t = 500\,\mathrm{ts}$. Two waves are created due to drop collision onto the liquid surface ($t = 1000\,\mathrm{ts}$). It is worth mentioning that during a drop collision on a liquid layer, the layer and liquid in the collision zone oscillate furiously. This is significantly affected by the intermittent conversion between potential and kinetic energies. With more time increasing (*i.e.* $t = 1500\,\mathrm{ts}$), a converging section is observed on the surface of the liquid.

Figure 5 shows a normal drop collision to the liquid surface at $R_{\mathrm{dp}} = 12\,\mathrm{Lu}$, $H = 0.5\,\mathrm{L}$, initial normal velocity of the drop $= -0.2\,\mathrm{Lu/ts}$, and We $= 32.5$ for different time steps. This figure is obtained at lower values of drop radius and Weber number in comparison with the previous figure. It is obvious that the required time to drop impact onto the liquid film increases with decrease in drop radius and Weber number due to the increase in the ratio of the drop

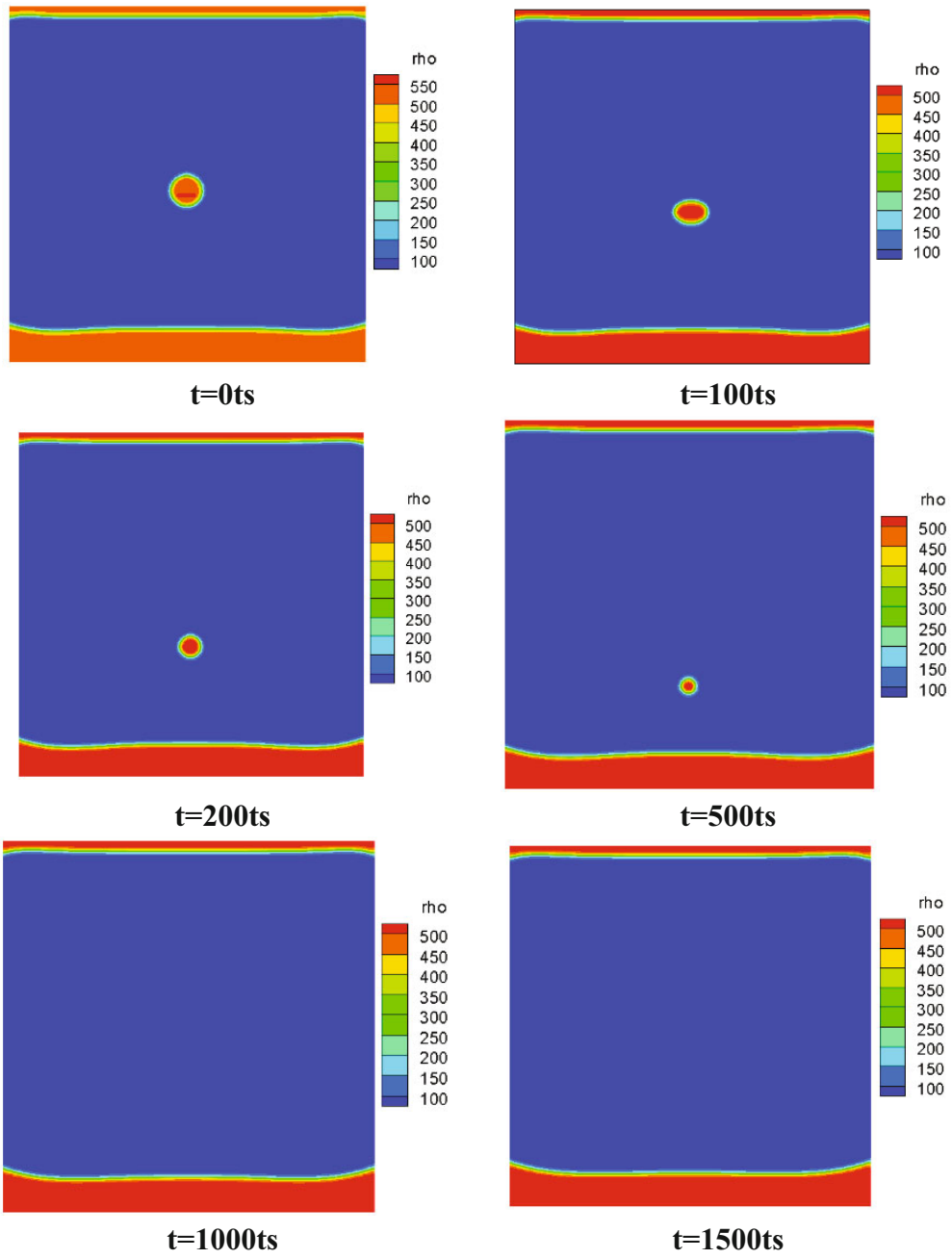


**Fig. 6.** Normal drop collision to the liquid surface at $R_{\mathrm{dp}} = 7\,\mathrm{Lu}$, initial normal velocity of the droplet $= -0.2\,\mathrm{Lu/ts}$, We $= 19$, and $H = 0.5\,\mathrm{L}$ for different time steps.

distance from the liquid film to the drop radius. Note that the drop velocity decreases with decrease in the Weber number. The deformation of the drop due to the sudden initial velocity is visible at $t = 100\,\mathrm{ts}$. This deformation converts the shape of the drop from a circle to an ellipse. With more time increasing (*i.e.* $t = 200\,\mathrm{ts}$), this deformation continues with the decrease in velocity due to the drag force. The effects of the drop in velocity can be seen before the collision of the drop onto the liquid film at $t = 500\,\mathrm{ts}$ (compare with previous figure at $t = 500\,\mathrm{ts}$). In this case due to the decrease in velocity and subsequently in drag force, the shape of the drop converts to the initial case (circle shape). However, the radius of the drop is decreasing due to evaporation. After collision, things are similar to the previous figure with weaker waves.

Figure 6 considers smaller values for the drop radius, $R_{\mathrm{dp}} = 7\,\mathrm{Lu}$, and Weber number We $= 19$ in comparison with the previous figure. In this case, the evaporation overcomes condensation and the drop evaporates and vanishes before collision onto the liquid surface due to the increase in the ratio of the drop distance from the liquid film to the drop radius. Note that the drop evaporates and vanishes for the drop radius less than a critical value.

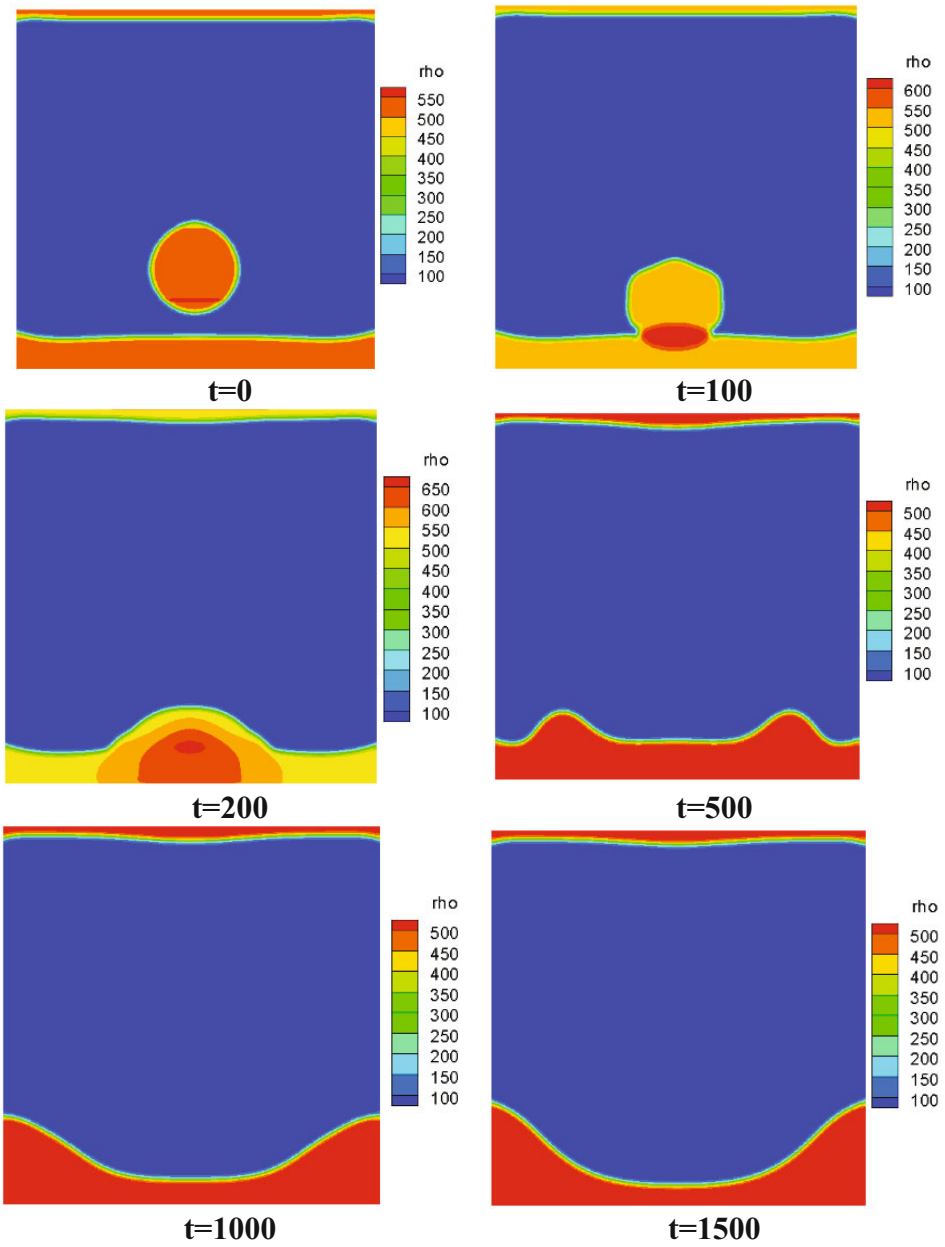


**Fig. 7.** Normal drop collision onto the liquid surface at $R_{\mathrm{dp}} = 22\,\mathrm{Lu}$, initial normal velocity of the drop $= -0.2\,\mathrm{Lu/ts}$, We $= 59.5$, and $H = 0.25\,\mathrm{L}$ for different time steps.

Figure 7 shows normal drop collision onto the liquid surface at $R_{\mathrm{dp}} = 22\,\mathrm{Lu}$, initial normal velocity of the drop $= -0.2\,\mathrm{Lu/ts}$, We $= 59.5$, and $H = 0.25\,\mathrm{L}$ for different time steps. It should be stated that this change in the initial position of the drop in comparison with fig. 4 has no influence on the initial deformation of the drop because the initial deformation occurs only due to the sudden change in the initial velocity of the drop. Moreover, the drop is only affected by the drag force during the falling process, but also the elapsed time due to the small distance between the drop and the liquid film surface is an important issue. Accordingly, there is not a significant deformation for the drop before collision in comparison with the case of $H = 0.5\,\mathrm{L}$ (see $t = 100\,\mathrm{ts}$). As compared with fig. 4, the height of the converging section, formed after collision, increases with the decrease in distance between the drop and the liquid film surface.

Figure 8 displays inclined drop collision to the liquid surface at $R_{\mathrm{dp}} = 22\,\mathrm{Lu}$, initial normal and horizontal velocity of the droplet $= 0.2\,\mathrm{Lu/ts}$ and $0.1\,\mathrm{Lu/ts}$, respectively, We $= 72$, and $H = 0.25\,\mathrm{L}$ for different time steps. It should be stated that the drop collides with the liquid film with an inclined angle (26.5° from normal direction) in this case. A different deformation is observed for this case in comparison to the previous cases due to the changes in collision angle and Weber number (see $t = 100\,\mathrm{ts}$). It can be seen that a stronger wave forms in the liquid film after collision of the drop in this case (see figure for $t = 200\,\mathrm{ts}$). By further time increasing (*e.g.*, $t = 1000\,\mathrm{ts}$), this wave transfers to the right direction of the computational area. Note that this is due to the changes in collision angle and Weber number.

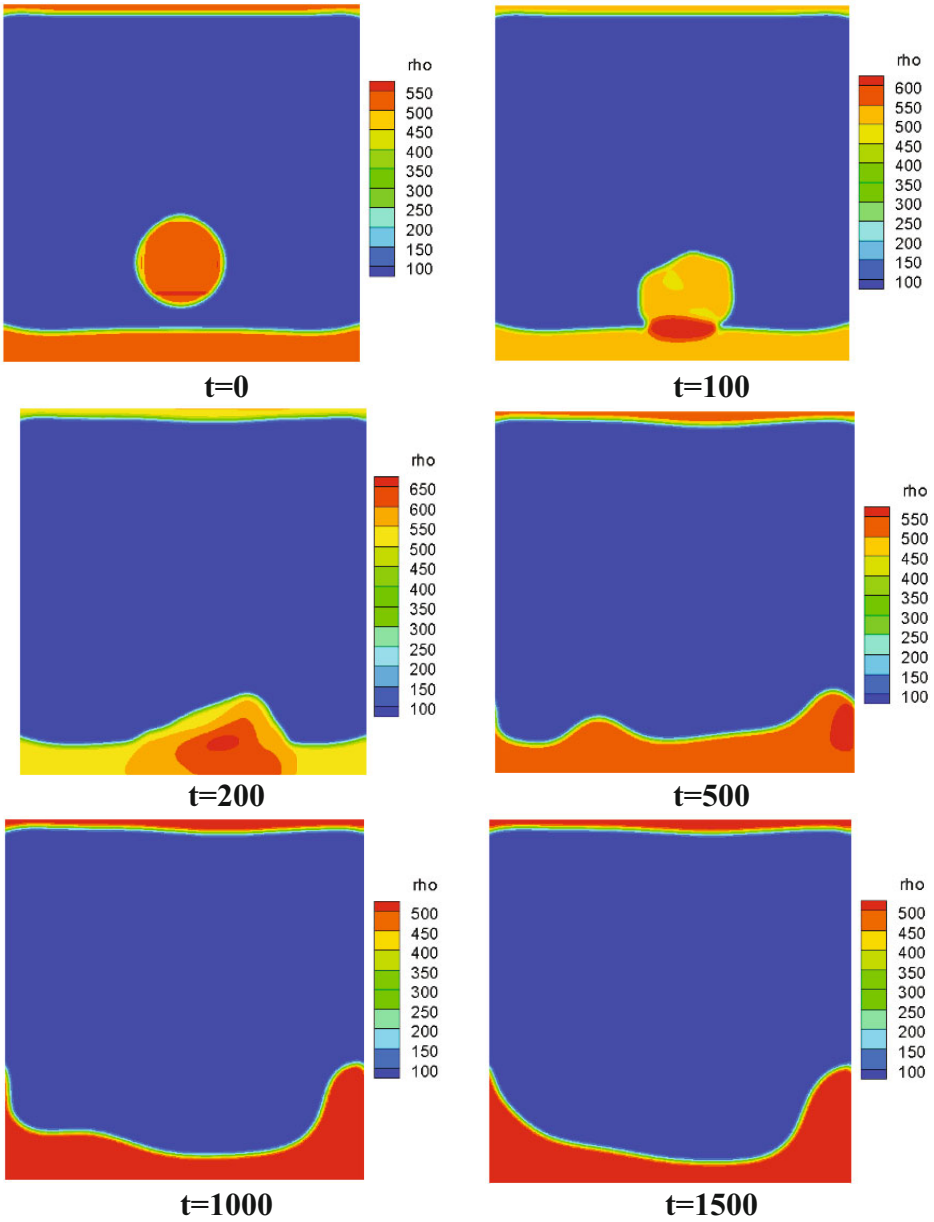


**Fig. 8.** Inclined drop collision to the liquid surface at $R_{\mathrm{dp}} = 22\,\mathrm{Lu}$, initial normal velocity of the droplet $= 0.22\,\mathrm{Lu/ts}$, We $= 72$, and $H = 0.25\,\mathrm{L}$ for different time steps.

Figure 9 presents the maximum height of created wave after the drop collision at different drop radiuses and initial positions of the drop. Results are presented for both normal and inclined collisions. As shown in this figure, the maximum height of created wave increases with the increase in drop radius for all cases. Moreover, the maximum height of created wave increases with the decrease in distance between the initial position of the drop and the liquid film surface. For example, there is 5.5% increment in the maximum height of created wave for $R_{\mathrm{dp}} = 22\,\mathrm{Lu}$ and normal collision when the initial position of the drop falls from $H = 0.5\,\mathrm{L}$ to $H = 0.25\,\mathrm{L}$. Longer waves are created when the drop collides with an inclined angle rather than a normal angle. For example, there is 14.7% increment in the maximum height of created wave for $R_{\mathrm{dp}} = 22\,\mathrm{Lu}$ when the collision of the drop changes from the normal situation to the inclined one.

Figure 10 shows the length fraction at different drop radiuses and initial positions of the drop. Note that the length fraction is specified as the ratio of the average amplitude of the wave (a) to the length between the two waves (b). It is observed that the length fraction reduces with the increase in drop radius for $H = 0.25\,\mathrm{L}$ and normal collision. For example, there is 40.85% reduction in length fraction for $H = 0.25\,\mathrm{L}$ and normal collision at $7\,\mathrm{Lu} < R_{\mathrm{dp}} < 22\,\mathrm{Lu}$. For normal collision, the length fraction increases with the decrease in distance between the initial position of the drop and the liquid film surface for drop radiuses 7 Lu and 22 Lu, vice versa for the case of $R_{\mathrm{dp}} = 12\,\mathrm{Lu}$.

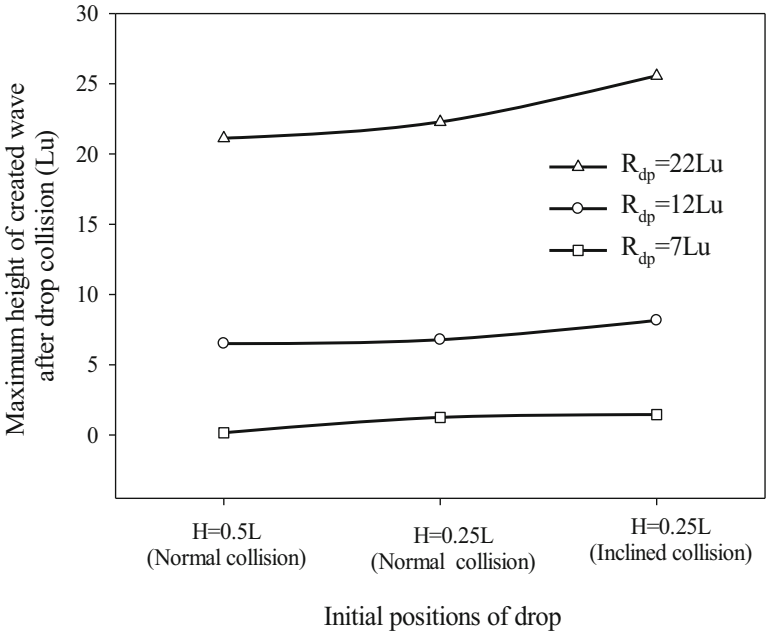


**Fig. 9.** Maximum height of the wave created after drop collision at different drop radiuses and initial positions of the drop.

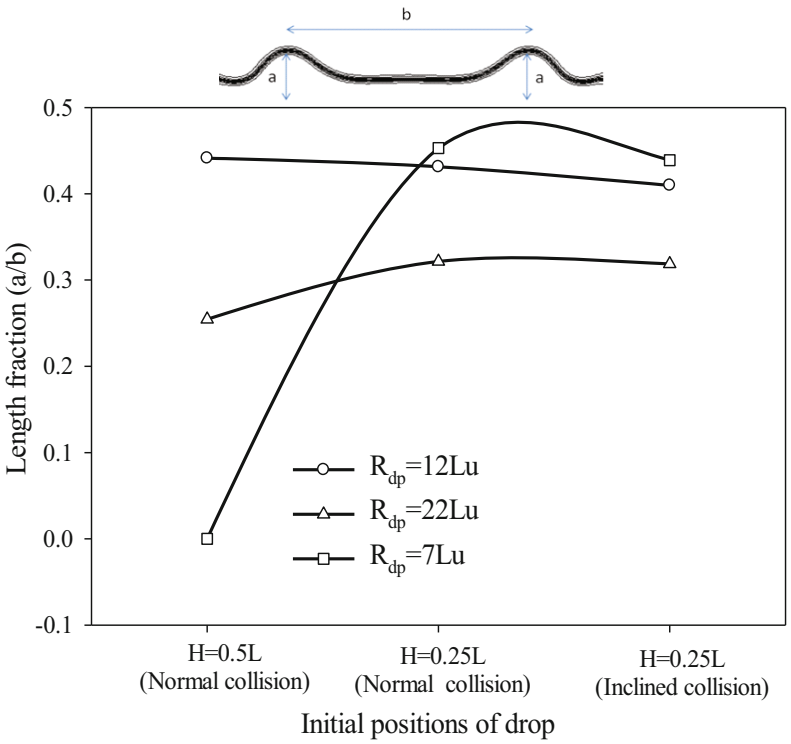


**Fig. 10.** Length fraction at different drop radiuses and initial positions of the drop.

For example, there is 26.4% increment in the length fraction for $R_{\mathrm{dp}} = 22\,\mathrm{Lu}$ and normal collision when the initial position of the drop falls from $H = 0.5\,\mathrm{L}$ to $H = 0.25\,\mathrm{L}$. Finally, the length fraction decreases when the collision of the drop changes from the normal situation to the inclined one for all the drop radiuses. For example, there is 2.2% reduction in the length fraction for $R_{\mathrm{dp}} = 22\,\mathrm{Lu}$ when the collision of the drop changes from the normal situation to the inclined one.

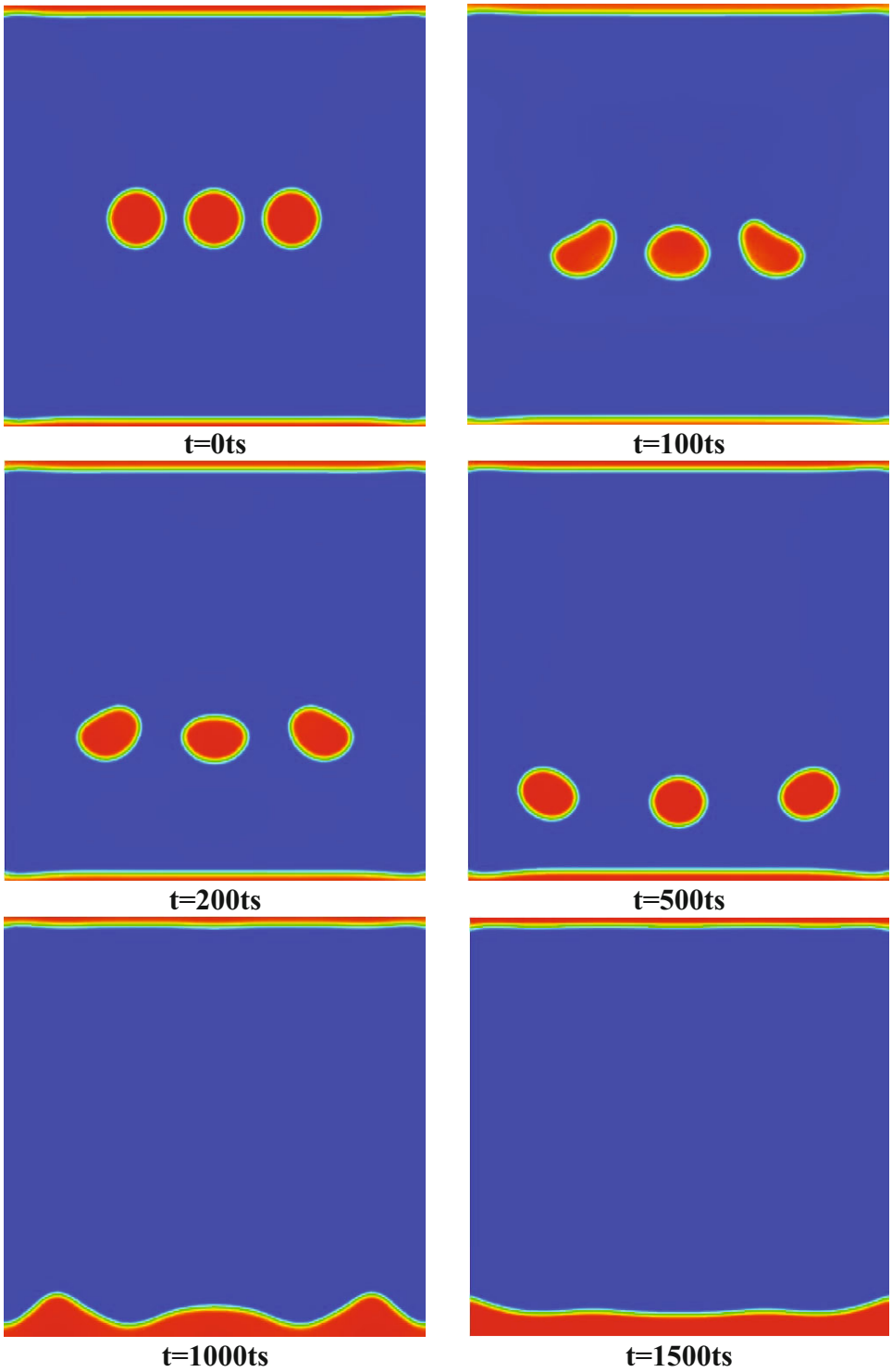


**Fig. 11.** Normal collisions of three drops to the liquid surface at $R_{\mathrm{dp}} = 12\,\mathrm{Lu}$, initial normal velocity of the central drop $= -0.2\,\mathrm{Lu/ts}$, initial velocity of lateral drops $= 0.22\,\mathrm{Lu/ts}$, and $H = 0.5\,\mathrm{L}$ for different time steps.

Figure 11 exhibits the normal collisions of three drops to the liquid surface at $R_{\mathrm{dp}} = 12\,\mathrm{Lu}$, initial normal velocity of the central drop $= -0.2\,\mathrm{Lu/ts}$, initial velocity of lateral drops $= 0.22\,\mathrm{Lu/ts}$, and $H = 0.5\,\mathrm{L}$ for different time steps. Moreover, the normal collisions of three drops to the liquid surface at $R_{\mathrm{dp}} = 12\,\mathrm{Lu}$, initial normal velocity of the central drop $= -0.2\,\mathrm{Lu/ts}$, initial velocity of lateral drops $= 0.22\,\mathrm{Lu/ts}$, and $H = 0.5\,\mathrm{L}$ for different time steps are plotted in fig. 12. Figure 11 shows the results in which the droplets are moving away from each other, while fig. 12 shows the results in which the droplets are approaching each other. Note that, in both figures, all the three drops are

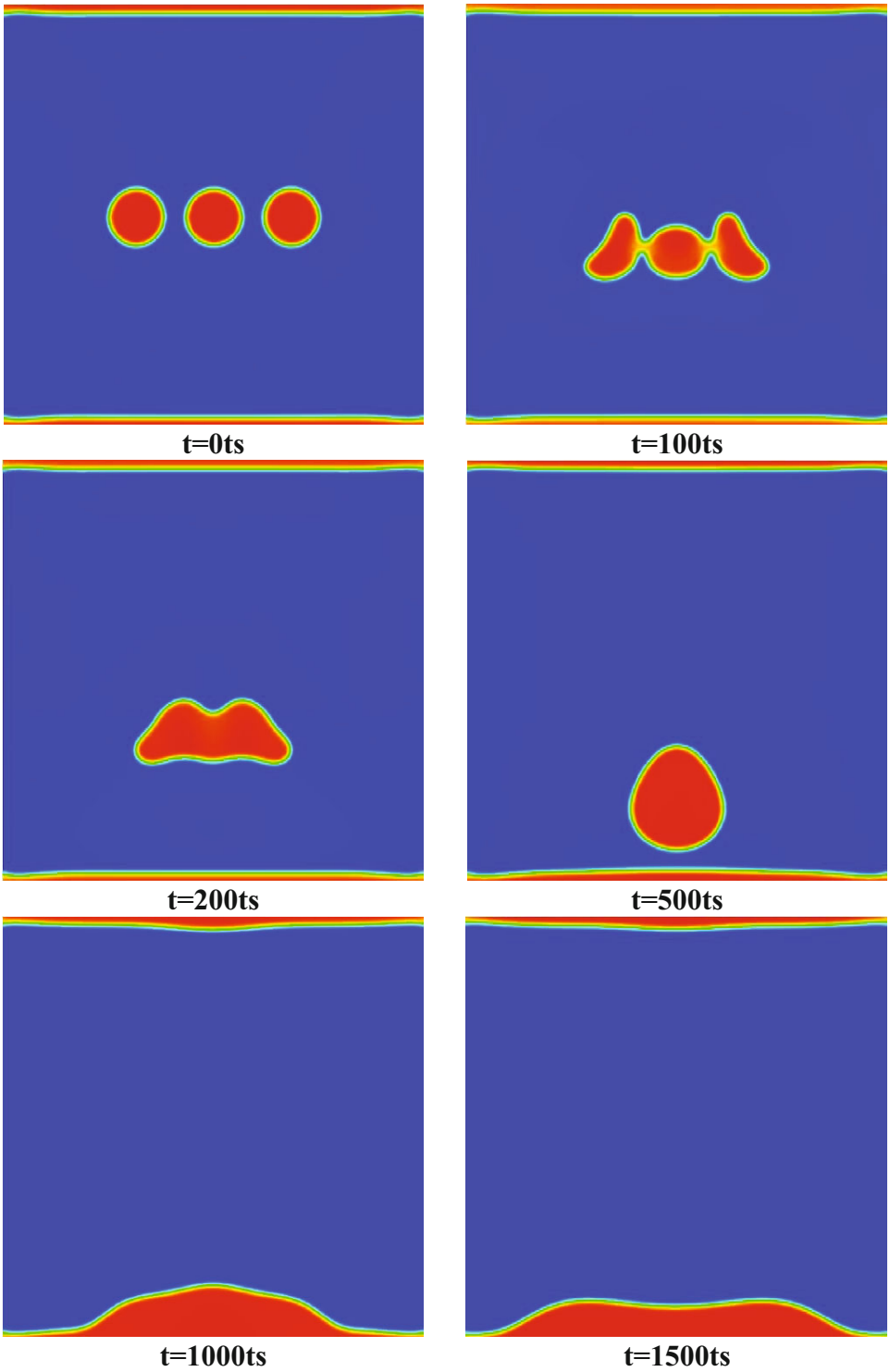


**Fig. 12.** Normal collisions of three drops to the liquid surface at $R_{\mathrm{dp}} = 12\,\mathrm{Lu}$, initial normal velocity of the central drop $= -0.2\,\mathrm{Lu/ts}$, initial velocity of lateral drops $= 0.22\,\mathrm{Lu/ts}$, and $H = 0.5\,\mathrm{L}$ for different time steps.

located in the middle position for the initial time. One of the important applications of drop collisions is surface coating using spray. However, since the motion of droplets in the spray coating is not predictable, it is generally possible to divide droplets moving in the two general cases including away from or adjacent to each other. As shown in fig. 11, the droplets do not touch each other in the direction of motion when they are moving away from each other. However, as shown in fig. 12, the coalescence between droplets occurs and a bulk of droplet is created before getting in contact the droplets with the surface when the droplets are approaching each other. In this case, a uniform coating cannot be formed and this is disadvantageous.

## Conclusion

The deformation and drop collision onto a liquid film in a saturated medium by LBM is simulated. The influences of important parameters such as drop radius, initial position of the drop, Weber number and the collision angle in this process are studied in details. The consequential outcomes from this study are listed as follows:

- The required time to impact the drop onto the liquid film increases with the decrease in drop radius and Weber number.
- For $R_{\mathrm{dp}} = 7\,\mathrm{Lu}$ and $\mathrm{We} = 19$, the evaporation overcomes condensation and the drop evaporates and vanishes before collision onto the liquid surface due to the increase in the ratio of the drop distance from the liquid film to the drop radius.
- A stronger wave forms in the liquid film after collision of the drop for the case of inclined collision in comparison with the normal one.
- There is 5.5% increment in the maximum height of the created wave for $R_{\mathrm{dp}} = 22\,\mathrm{Lu}$ and normal collision when the initial position of the drop falls from $H = 0.5\,\mathrm{L}$ to $H = 0.25\,\mathrm{L}$.
- There is 14.7% increment in the maximum height of the created wave for $R_{\mathrm{dp}} = 22\,\mathrm{Lu}$ when the collision of drop changes from the normal situation to inclined one.
- There is 40.85% reduction in the length fraction due to the increase in drop radius for $H = 0.25\,\mathrm{Lu}$ and normal collision at $7\,\mathrm{Lu} < R_{\mathrm{dp}} < 22\,\mathrm{Lu}$.
- There is 26.4% increment in length fraction for $R_{\mathrm{dp}} = 22\,\mathrm{Lu}$ and normal collision when the initial position of the drop falls from $H = 0.5\,\mathrm{L}$ to $H = 0.25\,\mathrm{L}$.
- There is 2.2% reduction in the length fraction for $R_{\mathrm{dp}} = 22\,\mathrm{Lu}$ when the collision of the drop changes from the normal situation to the inclined one.

## References


1. Y. Fu *et al.*, Chem. Eng. Process. **119**, 34 (2017).
2. S. Chen *et al.*, Chem. Eng. Process. **76**, 60 (2014).
3. A. Asadollahi, S. Rashidi, J.A. Esfahani, Meccanica **52**, 2265 (2016).
4. S. Chandra, C.T. Avedisian, Proc. R. Soc. London A **458**, 2417 (2002).
5. J. Fukai *et al.*, Phys. Fluids **7**, 236 (1995).
6. M. Francois, W. Shyy, Num. Heat Transf., Part B **44**, 119 (2003).
7. H. Fujimoto *et al.*, Int. J. Multiphase Flow **36**, 620 (2010).
8. S. Mitra *et al.*, Chem. Eng. Sci. **100**, 105 (2013).
9. S.L. Manzello, J.C. Yang, Exp. Fluids **32**, 580 (2002).
10. G.E. Cossali, A. Coghe, M. Marengo, Exp. Fluids **22**, 463 (1997).
11. R. Rioboo *et al.*, Exp. Fluids **35**, 648 (2003).
12. N. Nikolopoulos, J. Comput. Phys. **225**, 322 (2007).
13. T. Okawa, T. Shiraishi, T. Mori, Exp. Fluids **41**, 965 (2006).
14. M. Marengo *et al.*, Curr. Opin. Colloid Interface Sci. **16**, 292 (2011).
15. G. Liang *et al.*, Int. Commun. Heat Mass Transf. **54**, 67 (2014).
16. G. Liang *et al.*, Num. Heat Transf., Part B **69**, 575 (2016).
17. M. Marin, Math. Probl. Eng. **2008**, 1 (2008).
18. M. Marin, Meccanica **51**, 1127 (2016).
19. M. Marin, D. Baleanu, Bound. Value Probl. **111**, 1 (2016).
20. A. Zeeshan, R. Ellahi, Hassan, Eur. Phys. J. Plus **129**, 261 (2014).
21. Y. Wang *et al.*, Eur. Phys. J. Plus **130**, 9 (2015).
22. H.A. Tighchi, M. Sobhani, J.A. Esfahani, Eur. Phys. J. Plus **133**, 8 (2018).
23. J. Abolfazli Esfahani, A. Norouzi, Physica A **393**, 51 (2014).
24. M. Sbragaglia *et al.*, Phys. Rev. Lett. **97**, 2045031 (2006).
25. M.E. Cates *et al.*, Soft Matter **5**, 3791 (2009).
26. Y. Liu *et al.*, Nat. Phys. **10**, 515 (2014).
27. S. Leclaire *et al.*, Appl. Math. Modell. **40**, 6376 (2016).
28. A. Asadollahi, S. Rashidi, J.A. Esfahani, Meccanica **53**, 803 (2018).
29. M. Sheikholeslami, R. Ellahi, Z. Naturforsch. A **70**, 115 (2015).
30. S. Alapati, S. Kang, Y.K. Suh, in *Proceedings of the 3rd IASME/WSEAS International Conference on Continuum Mechanics*, edited by S. Sohrab *et al.* (WSEAS Press, 2008) p. 150.
31. J.J. Huang, C. Shu, Y.T. Chew, Phys. Fluids **21**, 0221031 (2009).
32. W. Wang *et al.*, Chem. Engin. J. **173**, 828 (2011).
33. X. Fu, Zhaohui Y.P. Hao, Langmuir **30**, 14048 (2014).
34. M.E.A.B. Amara, S.B. Nasrallah, Int. J. Hydrogen Energy **40**, 1333 (2015).

35. S. Zi-yuan *et al.*, J. Hydrodyn. **20**, 267 (2008).
36. S. Fallah Kharmiani, M. Passandideh-Fard, H. Niazmand, J. Mol. Liq. **222**, 1172 (2016).
37. X. Shan, H. Chen, Phys. Rev. E **47**, 1815 (1993).
38. X. Shan, Phys. Rev. E **73**, 1 (2006).
39. Y. Qian, D. d'Humières, P. Lallemand, Europhys. Lett. **17**, 1 (1992).
40. D.A. Wolf-Gladrow, *Lattice-Gas Cellular Automata and Lattice Boltzmann Models* (Springer Science & Business Media, New York, 2000).
41. S. Succi, *The Lattice Boltzmann equation for fluid dynamics and beyond* (Oxford University Press, 2001).
42. X. He, G.D. Doolen, J. Stat. Phys. **107**, 309 (2002).
43. N.S. Martys, H. Chen, Phys. Rev. E **53**, 743 (1996).
44. M.C. Sukop, D.T. Thorne Jr., *Lattice Boltzmann Modeling* (Springer, Berlin, Heidelberg, 2006).
45. D. Philip *et al.*, *Microdroplet Technology: Principles and Emerging Applications in Biology and Chemistry* (Springer Science & Business Media, New York, 2012).